Industrial Chemistry & Materials

ROYAL SOCIETY OF CHEMISTRY

PAPER

View Article Online
View Journal | View Issue

Cite this: *Ind. Chem. Mater.*, 2024, **2**, 328

Stable zinc anode by regulating the solvated shell and electrode–electrolyte interface with a sodium tartrate additive†

Jie Ren, Hai-Yang Wu, Wen Yan, Peng Huang * and Chao Lai *

Aqueous zinc-ion batteries (ZIBs) have attracted great research interest for use in large-scale energy storage devices due to their inherent safety, environmental friendliness, and low cost. Unfortunately, dendrite growth and interfacial side reactions during the plating/stripping process triggered by uneven electric field distribution on the surface of the Zn anode seriously hinder the further development of aqueous ZIBs. Here, practical and inexpensive sodium tartrate (STA) is used as an electrolyte additive to construct a stable electrode–electrolyte interface, in which STA adsorbs preferentially on the Zn metal surface, contributing to promoting homogeneous Zn deposition. Moreover, STA interacts more strongly with Zn^{2+}, which takes the place of the water molecules in the solvated shell and prevents the development of side reactions. In symmetrical cells and full cells, flat Zn anodes can therefore demonstrate remarkable cycle stability, opening the door for the development of cost-effective and effective electrolyte engineering techniques.

Received 16th October 2023,
Accepted 4th December 2023

DOI: 10.1039/d3im00111c

rsc.li/icm

Keywords: Zinc ion battery; Electrolyte additive; Zinc dendrites; Hydrogen evolution reaction; Anode protection.

1 Introduction

The unsustainable growth of human society is hampered by the major environmental issues that result from the overuse of fossil fuels. Recently, a double carbon goal of "emission peak and carbon neutrality" has been put forward for the development of renewable energy sources.[1–3] Modern energy storage facilities must be built as soon as possible.[4] At present, lithium-ion batteries (LIBs) that drive portable electronic devices and electric vehicles are the most widely used in the energy storage field.[5–7] But so far, there remain a number of concerns, such as high costs, toxic electrolytes, and inadequate safety, which substantially impede the use of large-scale energy storage.[8,9] Compared with organic electrolytes used in lithium-ion batteries, aqueous electrolytes are environmentally friendly and non-flammable, and have high ionic conductivity. Aqueous ZIBs stand out from other metal-ion batteries (*e.g.* aluminum,[10] potassium,[11] sodium[12]) and have aroused a great deal of attention and interest due to their lower redox potential (−0.76 V *vs.* standard hydrogen electrode), higher theoretical capacity (820 mA h g^{-1}, 5854 mA h L^{-1}), higher natural abundance and lower cost.[13–17] In short, aqueous ZIBs are considered the most promising alternatives to LIBs.

Notwithstanding these advantages, interfacial side reactions (such as corrosion and hydrogen evolution)[18–20] and growth of Zn dendrites,[21–23] which occur throughout the reversible cycle, limit the practical applicability of aqueous ZIBs and result in low coulombic efficiency (CE) and poor long-term cycle stability.[24] Due to the "tip effect", where protuberance of the electrode surface shows a stronger electric field, Zn^{2+} is inclined to deposit at tips, forming irregular Zn dendrites.[25] Further growth of dendrites can puncture the diaphragm and eventually result in a short-circuit of batteries.[26,27] Also, as soon as the weakly acidic electrolyte comes into contact with the metal Zn, corrosion starts to take place. The Zn anode and electrolyte are consumed to produce insulating by-products and H_2.[28] Meanwhile, Zn^{2+} in the $ZnSO_4$ electrolyte exists in the form of a solvated structure $[Zn(H_2O)_6^{2+}]$,[29] and water molecules as electron acceptors around the Zn^{2+} will decompose inevitably during the Zn^{2+} deposition ($2H_2O + 2e^- = 2OH^- + H_2\uparrow$). Moreover, the hydrogen evolution reaction (HER) will cause a change in the local pH value, resulting in increased battery internal pressure and electrolyte leakage. The generated OH^- will participate in the reaction and form electrochemical inert by-products (such as $Zn_4(OH)_6SO_4{\cdot}xH_2O$),[30–33] which

School of Chemistry and Materials Chemistry, Jiangsu Normal University, Xuzhou, Jiangsu, 221116, China. E-mail: huangpeng@jsnu.edu.cn, laichao@jsnu.edu.cn

† Electronic supplementary information (ESI) available. See DOI: https://doi.org/10.1039/d3im00111c

effectively stop the transfer of ions at the interface and reduce coulombic efficiency (CE) directly.

Several different Zn anode protection solutions have been put out to address these issues. These strategies are largely classified into the following categories: adding electrolyte additives,[34,35] designing electrode structures,[36–40] constructing artificial interface layers[21,41,42] and modifying the diaphragm.[43,44] To enhance the Zn anode that may be utilized in large-scale manufacturing and use, one of the strategies is the use of electrolyte additives. It is reported that trace amounts of polyethylene oxide (PEO),[39] polyethylene glycol (PEG),[45] or polyacrylamide (PAM)[46] are added into the $ZnSO_4$ electrolyte and adsorbed on the Zn surface, which promotes the uniform nucleation of Zn and is conducive to the homogenization of the deposition layer. In addition, EDTA-2Na,[47] methanol (CH_3OH),[30] or dimethyl sulfoxide (DMSO)[48] is introduced into the $ZnSO_4$ electrolyte to adjust the solvated shell of Zn^{2+} ($[Zn(H_2O)_6]^{2+}$), which suppresses the occurrence of side reactions in the electrode–electrolyte interface. Therefore, it is necessary to develop multi-functional electrolyte additives for the electrode protection of ZIBs. By modulating the solvation structure and the deposition morphology of Zn, multiple effects can be achieved. This can not only inhibit dendrites but also reduce side reactions, which is crucial for the construction of safer and more efficient ZIBs.

In coordination chemistry, sodium tartrate (STA) is used as a chelating agent for metal ions. It has an excellent ability to chelate most divalent and trivalent metal ions.[49] Herein, sodium tartrate is proposed as a novel organic electrolyte additive for ZIBs to suppress the formation of dendrites and reduce side reactions (mainly suppression of hydrogen evolution), constructing a stable electrode–electrolyte interface. Combining the experimental results and theoretical calculation, it is found that a stronger adsorption energy between STA and the Zn metal surface induces preferential adsorption of STA on Zn foil, inhibiting the growth of dendrites. Thus, the STA molecule and Zn^{2+} have a stronger binding than H_2O to allow STA to replace water molecules and reconstruct the solvation structure of Zn^{2+}, which effectively reduces the decomposition of active water molecules. It's worth noting that the content of hydrogen precipitation can be monitored in real time by gas chromatography, which is a good indication that STA has the ability to inhibit hydrogen production. Due to these multiple functions, symmetrical cells and full cells using STA exhibit excellent cycle stability, superior to those using a pure $ZnSO_4$ electrolyte.

2 Results and discussion

In pure $ZnSO_4$ electrolyte, due to the uneven distribution of electric field caused by the unsmooth surface of Zn foil, Zn^{2+} prefers to aggregate at nucleation sites, forming two-dimensional diffusion protuberance. Under the further action of the "tip effect", the growth of dendrites is intensified, and then the membrane is punctured, resulting in a short circuit of the battery, which greatly reduces the lifespan of the battery.[50] A multitude of side reactions (including hydrogen evolution, passivation, *etc.*) and by-products are produced as a result of the decomposition of many active water molecules in the electrolyte, which has an adverse impact on the battery's cycle stability and lifespan (Fig. 1a). In contrast, as shown in Fig. 1b, after STA is added to the $ZnSO_4$ electrolyte, on the one hand, since the interaction between sodium tartrate and Zn^{2+} is greater than that between Zn^{2+} and water molecules, it can replace the water molecules around Zn^{2+} and enter into the solvated shell, inhibiting the decomposition of active water molecules, and thus achieving the effect of suppressing hydrogen evolution. On the other hand, STA can be adsorbed on the surface of the Zn anode to form a uniform and dense film, which limits the two-dimensional diffusion behavior of Zn^{2+} and avoids the direct contact between the electrode and electrolyte interface, which plays a crucial role in inhibiting dendrite growth.

The effects of STA added into the $ZnSO_4$ electrolyte can be firstly verified by immersion experiments. The concentration gradient of the prepared STA in the electrolyte is as follows: (i) 0.1 g L^{-1} STA; (ii) 0.2 g L^{-1} STA; (iii) 0.5 g L^{-1} STA (Fig. S1†). As demonstrated in Fig. 1c–f, the Zn foil was soaked in pure $ZnSO_4$ ("blank electrolyte") and $ZnSO_4$ containing different concentrations of STA for 5 hours, and the Zn foil was taken out and rinsed with deionized water. The surface morphology of the Zn foil was examined by SEM after drying in an oven. In the absence of electrolyte additives, a large number of flake by-products with a certain size, such as $Zn_4(OH)_6SO_4{\cdot}xH_2O$,[51] were attached to the surface of Zn foil due to side reactions. But if 0.1 g L^{-1} STA was added to the $ZnSO_4$ electrolyte, the number and size of sheet by-products were significantly reduced. The Zn foil was shielded from corrosion as a result of a relatively small quantity of STA being adsorbed on its surface. When the concentration of STA increased to 0.2 g L^{-1}, there were almost no by-products on the surface of the Zn foil, and the Zn foil immersed seemed flatter and smoother, implying that the Zn foil has excellent cycle stability due to the formation of an adsorption layer. However, if the concentration of STA was increased to 0.5 g L^{-1}, by-products were restacked on the surface of the Zn foil, but it was still better than the blank electrolyte. This may be due to the fact that STA cannot form a continuous adsorption layer when it is inadequate, and that steric hindrance occurs when STA is present in excess, which prevents the uniform deposition of Zn^{2+}.[52]

To explore the functions of STA on the improved plating/stripping performance of the Zn anode, the physical properties of electrolytes with different concentrations of STA were investigated. As presented in Fig. 2a, with an increase in STA concentration, the ionic conductivity of the electrolytes steadily improved. This facilitated ion transport and charge transfer throughout the discharging and charging process. Corrosion resistance is an indicator of electrode–electrolyte interface stability. The Tafel curve was measured by cyclic

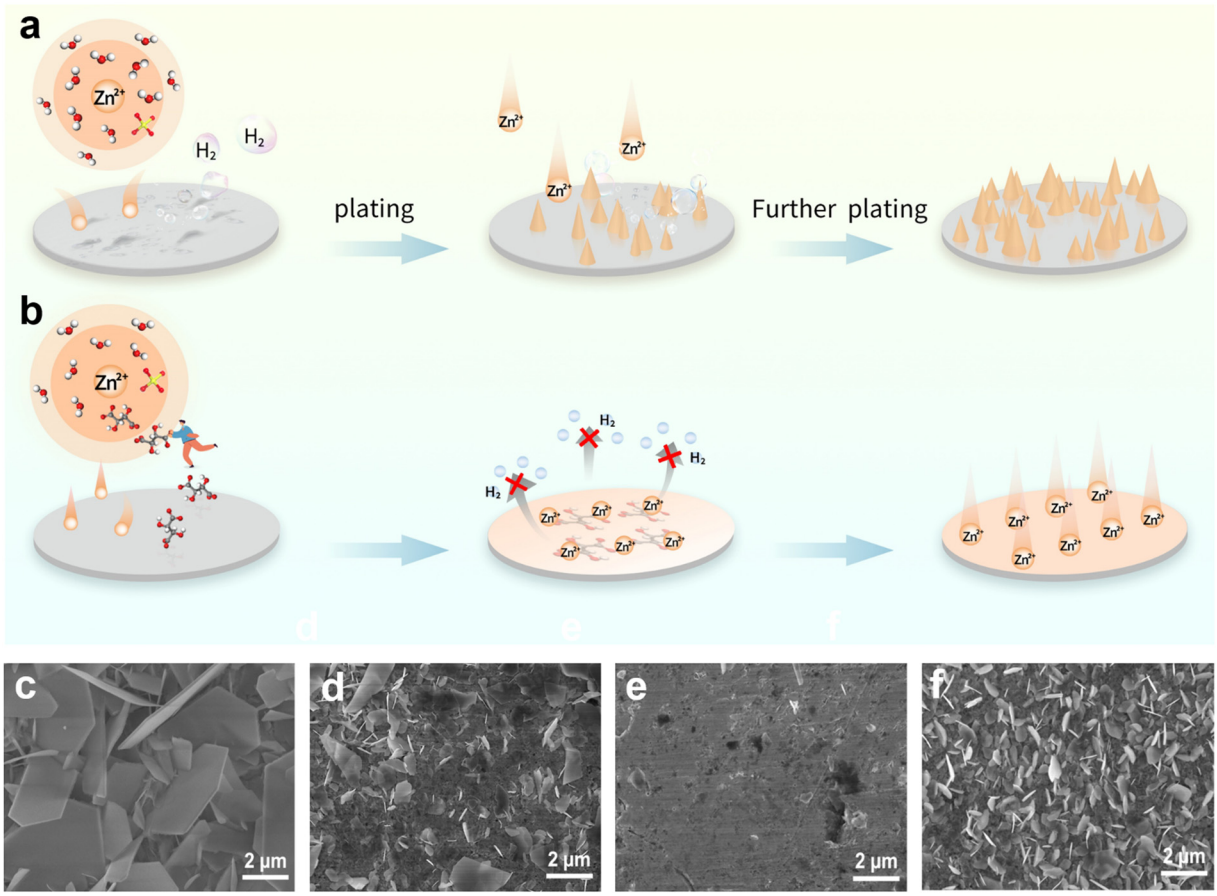

Fig. 1 Schematic illustration of the Zn deposition process in (a) $ZnSO_4$ and (b) $ZnSO_4$–STA electrolytes; (c–f) SEM images of Zn foil soaked for 5 hours in the $ZnSO_4$–STA electrolyte (0 g L^{-1}, 0.1 g L^{-1}, 0.2 g L^{-1}, and 0.5 g L^{-1}, respectively).

voltammetry to assess the anti-corrosion capability of the electrolyte. As demonstrated in Fig. 2b, the corrosion current decreases from 1.176 mV to 0.920 mV and then increases to 1.108 mV with the existence of STA in the $ZnSO_4$ electrolyte, confirming that the lower corrosion current alleviates the corrosion issue and avoids the formation of parasitic by-products.[53] In addition, the adsorption effect of STA on Zn was revealed *via* differential capacitance measurement, which directly affects the stability between the electrode and electrolyte interface, thus regulating the plating/stripping behavior.[54,55] As shown in Fig. 2c, compared to the blank electrolyte, the electrolyte containing STA has a reduced capacitance. When the concentration of STA is 0.2 g L^{-1}, the electrode capacitance shows the lowest value, demonstrating the formation of an adsorption layer that behaves like a protective film and equally covers the Zn foil's surface, which inhibits the corrosion behavior of the electrolyte and restricts Zn^{2+} ion flux, which is concordant with the results of the above immersion test. At the same time, the contact angle experiment further validates the affinity between the electrolyte and the Zn substrate (Fig. S2†).

A negative overpotential (−150 mV) is applied to the Zn electrode through the chronoamperometry method, further revealing the nucleation behavior and change of the Zn surface. As a result of an unregulated 2D diffusion process, the current in both the STA-containing and the blank electrolytes initially dropped off quickly. However, after 40 s, the current decline in the $ZnSO_4$–STA electrolyte became much less serious, which might be related to the Zn^{2+} 3D diffusion behavior, thus hindering the growth of dendrites and maintaining the smooth surface morphology (Fig. S3†).[56,57] In addition to preventing dendrite growth, STA additive adsorption also minimizes the occurrence of side reactions, particularly hydrogen evolution. To evaluate this, linear sweep voltammetry (LSV) scans were performed. As presented in Fig. 2d, the electrolyte with STA has a lower HER overpotential than the blank electrolyte at the same current density, manifesting that the addition of STA affected suppressing H_2 generation.

Symmetrical cells in 1 mol L^{-1} $ZnSO_4$ with various STA concentrations were built to more thoroughly assess how the addition of STA affected cycle stability and rate performance. As shown in Fig. 3a, the voltage profiles of Zn||Zn symmetrical cells in the blank electrolyte at a current density of 10 mA cm^{-2} with a capacity of 2 mA h cm^{-2} were recorded. The voltage of symmetrical cells working in the blank electrolyte presents fluctuation significantly after 103 hours, reflecting the internal short circuit in the battery, which is

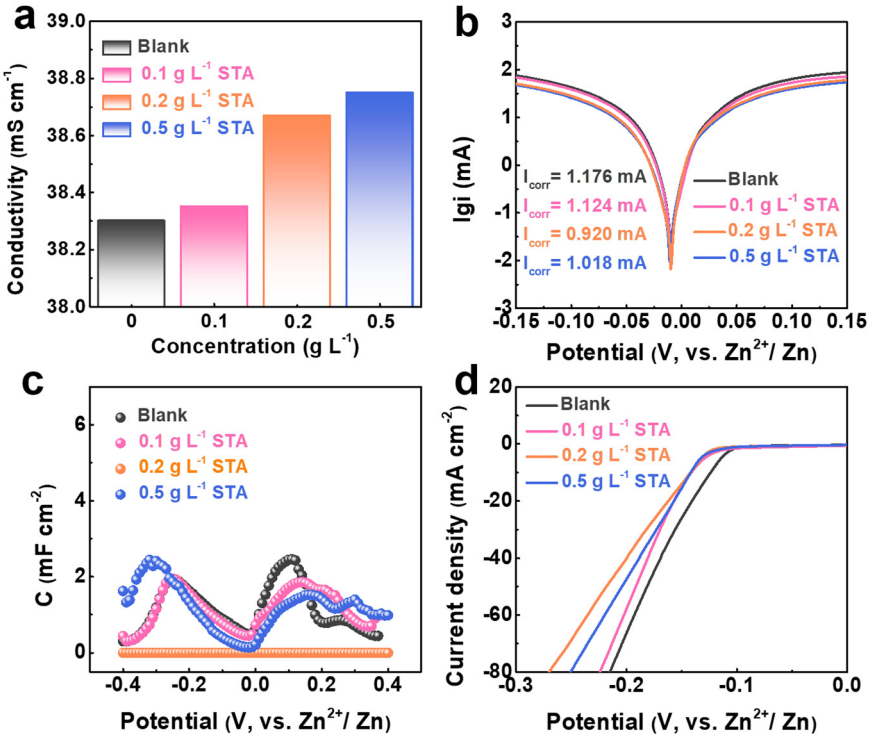

Fig. 2 (a) Ion conductivity of 1 mol L^{-1} $ZnSO_4$ and 1 mol L^{-1} $ZnSO_4$ containing different concentrations of STA; (b) the corresponding Tafel curves were recorded by scanning at 1 mV s^{-1} of three-electrode systems; (c) differential capacitance plots were obtained in the electrolyte with different amounts of STA; (d) linear sweep voltammetry curves measured in $ZnSO_4$ and $ZnSO_4$–STA systems.

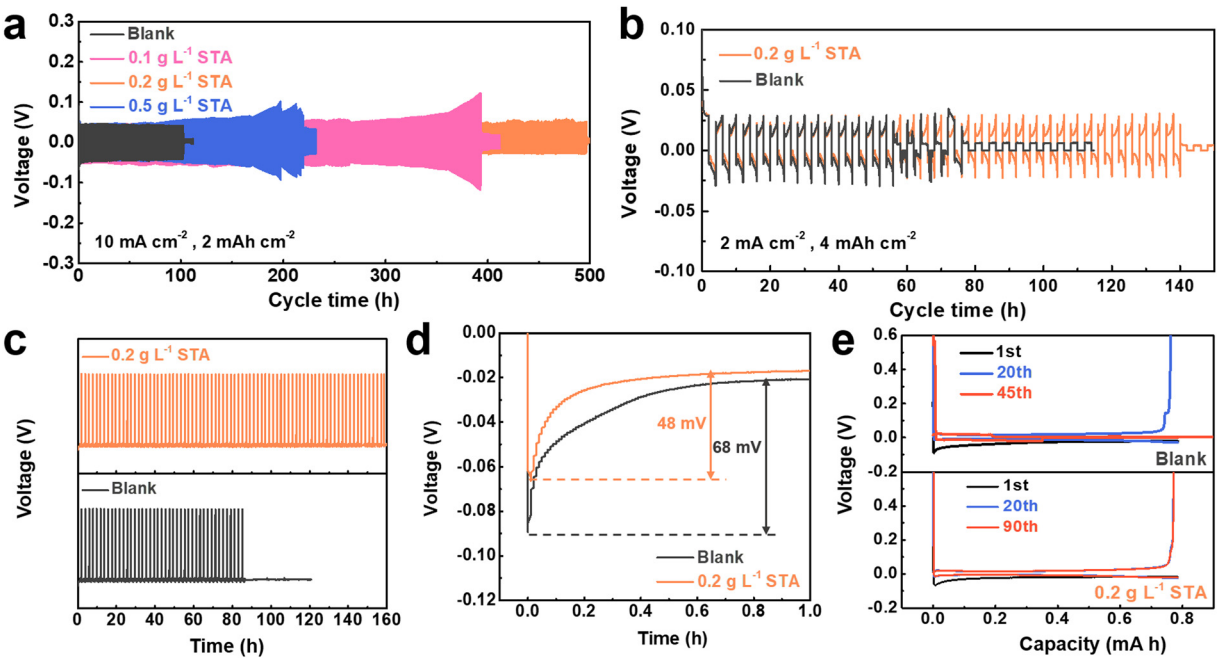

Fig. 3 (a) Cycling performance of Zn||Zn symmetric cells using 1 mol L^{-1} $ZnSO_4$ and 1 mol L^{-1} $ZnSO_4$ containing different concentrations of STA at a current density of 10 mA cm^{-2} with a fixed capacity of 2 mA h cm^{-2}; (b) voltage–time profiles of Zn||Zn symmetric cells in 1 mol L^{-1} $ZnSO_4$ with/without STA at 2 mA cm^{-2} with a capacity of 4 mA h cm^{-2}; (c) voltage profiles of Zn||Cu asymmetric cells in 1 mol L^{-1} $ZnSO_4$ with/without STA; (d) the initial nucleation potential for Zn||Cu asymmetric cells in the two electrolytes; (e) the corresponding voltage–capacity curves for the selected cycles in 1 mol L^{-1} $ZnSO_4$ with/without STA.

ascribed to the serious growth of dendrites. In comparison, the cycle life of the battery is increased to about 500 hours with the addition of 0.2 g L^{-1} STA. Furthermore, the Zn||Zn symmetrical cells with 0.1 g L^{-1} STA and 0.5 g L^{-1} STA deliver a cycling life of 384 hours and 217 hours, respectively. Consequently, the optimal concentration of STA is selected to be 0.2 g L^{-1} in the subsequent experiments. After that, symmetrical batteries with a capacity of 4 mA h cm^{-2} and a current density of 2 mA cm^{-2} were assembled for comparison, further demonstrating the viability of the battery cycle stability enhanced by the addition of STA. As illustrated in Fig. 3b, compared with the blank electrolyte, the cycle time of the symmetric battery assembled with 0.2 g L^{-1} STA is about twice as long as that of the blank electrolyte. The irregular dendrites coated on the surface of the Zn foil, which disrupt the distribution of the electric/ion field and cause the battery to short circuit, are likely to blame for the poor results in the pure $ZnSO_4$ electrolyte.[58,59] In addition, when the battery with two different electrolytes was run at a current density of 5 mA cm^{-2} and a capacity of 2 mA h cm^{-2}, the voltage of the battery in the blank electrolyte fluctuated and eventually shortcut at 130 hours (Fig. S4†). However, the modified electrolyte could be stably circulated for about 350 hours, confirming the superiority of STA. Electrochemical impedance spectroscopy (EIS) showed that the charge transfer resistance of the Zn||Zn symmetrical battery assembled with the electrolyte containing STA was smaller than that of the blank electrolyte (Fig. S5†). This may be because the interaction between Zn^{2+} and STA destroyed the solvated structure of Zn^{2+} and promoted the charge transfer of Zn^{2+}.

Coulombic efficiency (CE) is another important factor affecting the battery life.[60] By assembling Zn||Cu asymmetric cells with different electrolytes, plating/stripping tests were carried out at a current density of 1 mA cm^{-2} and a capacity of 1 mA h cm^{-2}. As presented in Fig. 3c, the battery using the blank electrolyte had a significant drop after only 80 hours. In contrast, the battery with 0.2 g L^{-1} STA could cycle stably for more than 160 hours, demonstrating that STA modulates the deposition/stripping process of Zn^{2+} regularly. Fig. 3d shows the initial nucleation potential tested with the two electrolytes in the Zn||Cu half cells. After the addition of the electrolyte additive (0.2 g L^{-1} STA), the nucleation potential is reduced from 68 mV in the blank electrolyte to 48 mV. Details of the voltage capacity curve for the Zn||Cu asymmetric cell in a fixed cycle can be represented by Fig. 3e. The CE of the Zn||Cu asymmetric cell using the blank electrolyte begins to decay at 20 cycles and finally fails at 45 cycles. In sharp contrast, the CE of the cell with 0.2 g L^{-1} STA remains stable over 90 cycles, indicating that the utilization rate of Zn during the cycling is relatively high and the side reaction is effectively inhibited.

In order to further clarify the regulation effect of STA on the electrode–electrolyte interface, characterization methods were used to analyze the composition and morphology of the surface of Zn foil. Top-view and cross-sectional scanning electron microscopy (SEM) images of the Zn anode after 10 cycles are shown in Fig. 4a–d. In the blank electrolyte, a great

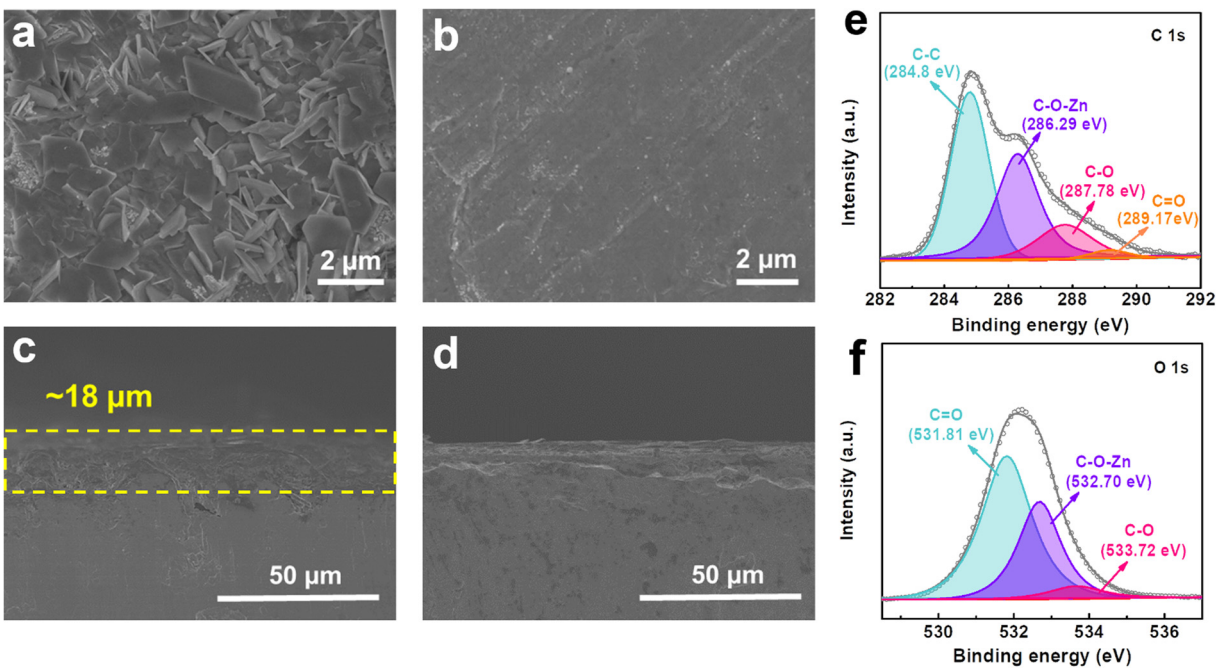

Fig. 4 Top-view SEM images of the Zn anode in 1 mol L^{-1} $ZnSO_4$ (a) and 1 mol L^{-1} $ZnSO_4$ with 0.2 g L^{-1} STA (b) after 10 cycles at a current density of 10 mA cm^{-2} and a capacity of 2 mA h cm^{-2}; cross-sectional SEM images of the Zn anode in 1 mol L^{-1} $ZnSO_4$ (c) and 1 mol L^{-1} $ZnSO_4$ with 0.2 g L^{-1} STA (d) after 10 cycles at a current density of 10 mA cm^{-2} and a capacity of 2 mA h cm^{-2}; XPS spectra of C 1s (e) and O 1s (f) of the Zn anode after 10 cycles with 0.2 g L^{-1} STA.

deal of flake-like dendrites and by-products can be observed to be disorderedly stacked on the surface of the Zn foil. Meanwhile, these dendrites will grow into the diaphragm to accelerate the degradation of battery performance or short circuits. In comparison, the Zn anode in the electrolyte containing STA presents a relatively flat and smooth surface, which intuitively confirms the uniform deposition of Zn during the plating/stripping process without unfavorable dendrite formation. The energy dispersive spectroscopy (EDS) element analysis on the surface of the Zn electrode after 10 cycles is shown in Fig. S6.† Elements C, O, S and Zn simultaneously detected uniformly disperse on the surface of Zn foil, which also evidences that STA is evenly adsorbed on the Zn anode and regulates the homogeneous Zn^{2+} deposition. Atomic force microscopy (AFM) is used to characterize the roughness of the surface of the Zn anode (Fig. S7†). It is clear that the height of the surface bulge of the Zn anode in the blank electrolyte is higher than that containing STA additives, which further proves that STA plays a role in uniform Zn deposition and inhibits the growth of dendrites. X-ray photoelectron spectroscopy (XPS) was further studied to support the view that STA chemically anchors on the surface of the Zn electrode. The total spectrum and Zn 2p spectrum can be obtained from the energy spectrum in Fig. S8.† As demonstrated in Fig. 4e and f, for the C 1s spectrum, the Zn foil treated with 0.2 g L^{-1} STA shows a new peak at 286.29 eV, which can be indexed to the C=O bond in STA. The peak at 532.70 eV in the O 1s spectrum can also be attributed to the C=O bond of STA. These results not only indicate that STA is stably anchored on the Zn surface, but also reveal the interaction between Zn and STA in the form of a C–O–Zn cross-linked structure. Fourier infrared (FT-IR) spectroscopy also further verified the presence of C–O–Zn cross-linked structures on the surface of the Zn electrode (Fig. S9†).[66] It can be observed that the characteristic peak of Zn–O is at 897 cm^{-1}, which proves that the Zn^{2+} forms a new bond with oxygen on the carbonyl group in STA.

DFT calculations were performed to further explain the interaction between Zn^{2+}, STA, and H_2O. From Fig. 5a, it can be seen that the binding energy of Zn^{2+}–STA is higher than that of Zn^{2+}–H_2O and STA–H_2O, further indicating that the STA molecule and Zn^{2+} have a stronger binding than H_2O to allow STA to replace water molecules and reconstruct the solvation structure of Zn^{2+}. The Raman spectra of different electrolytes further confirm the regulating effect of the solvation structure. In Fig. S10,† the peak at 982.07 cm^{-1} observed in the Raman spectrum of the 1 M $ZnSO_4$ electrolyte corresponds to the symmetrical stretching vibration of SO_4^{2-}($\nu(SO_4^{2-})$). With the 0.1 g L^{-1} STA additive, the peak shifted to higher frequencies at 984.09 cm^{-1}. The coordinated H_2O molecules in the solvation structure are partially replaced with STA, leading to weakened solvation between H_2O and Zn^{2+} as well as the regulated solvation sheath of $[Zn(H_2O)_6]^{2+}$. Fig. 5b directs the adsorption energy of H_2O and STA at different adsorption sites on the Zn (002) slab. Surprisingly, there is very little interaction between H_2O and

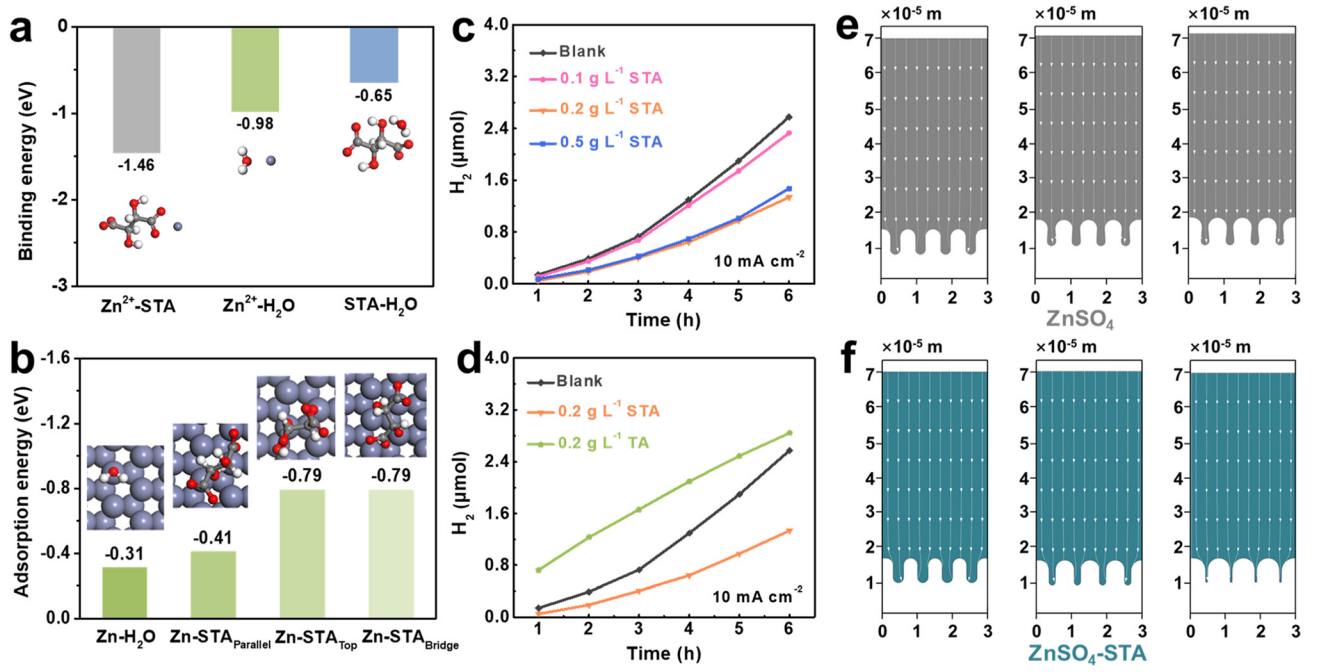

Fig. 5 (a) The binding energy for Zn^{2+} with different compounds (STA and H_2O) using DFT calculation; (b) adsorption energy of H_2O and STA molecules on the Zn (002) crystal plane at different adsorption sites; (c) graph of the hydrogen precipitated content with time in different electrolytes at a current density of 10 mA cm^{-2}; (d) comparison of the hydrogen evolution content of 0.2 g L^{-1} tartaric acid (TA) and STA with the blank electrolyte; finite element simulation (FEA) for the electrode–electrolyte interface at 0, 100 and 200 s (from left to right) in the 1 mol L^{-1} $ZnSO_4$ electrolyte (e) and 1 mol L^{-1} $ZnSO_4$ electrolyte with STA (f).

Zn foil, and H_2O positioned on the Zn (002) plane in the top position is the most stable ($E_{ads.}$ = −0.31 V). STA and Zn foil instead have significant interaction. The adsorption energy of STA placed vertically (including top, bridge, and hollow positions) along the surface of the Zn sheet is lower than that placed in the parallel position ($E_{ads.}$ = −0.79 V *vs.* 0.41 V) (H_2O and STA placed on the Zn (002) slab with other adsorption sites as shown in Fig. S11†). Therefore, STA prefers to adsorb on the Zn (002) slab in a vertical position. Finite element simulation (FEA) was also carried out to simulate the Zn plating/stripping process in different electrolyte systems. Gas chromatography was also employed to monitor the content of precipitated hydrogen in real time to further verify the effect of STA in inhibiting hydrogen evolution. The schematic diagram of the hydrogen evolution device is shown in Fig. S12.† As presented in Fig. 5c, by comparing the hydrogen evolution content of Zn foil in the blank electrolyte and electrolyte with different concentrations of STA, it is obvious that under the conditions of adding STA, the hydrogen content is reduced and the hydrogen content of electrolyte with 0.2 g L^{-1} STA is the lowest value. This illustrates that 0.2 g L^{-1} STA has the most significant inhibitory effect compared with the blank electrolyte, which is consistent with the cycling performance of symmetrical cells. Moreover, when the current density is set to 4 mA cm^{-2}, the same result is still obtained (Fig. S13†). In addition, comparing the hydrogen evolution content of tartaric acid with sodium tartrate, the results show that tartaric acid has the highest hydrogen evolution content. This could be a result of the tartaric acid solution's acidity, which encourages hydrogen precipitation (Fig. 5d). As demonstrated in Fig. 5e, in the blank electrolyte, the Zn anode presents an uneven surface due to the random deposition of Zn^{2+}, which leads to the rampant growth of Zn dendrites. However, before the Zn dendrites form, STA addition will preferentially adsorb on the Zn anode's surface, thereby shielding the tip electric field. At the same time, its adsorbed concentration is adjusted according to the surface curvature of the electrode, accelerating the filling of the concave surface,[61] so that the surface of the Zn foil is in a flat and uniform state (Fig. 5f).

The battery's electrochemical performance is also a significant marker of its commercial viability.[62] Therefore, V_2O_5 was used as a cathode and the Zn sheet as an anode to fabricate the full cell to verify the feasibility of adding STA. In the initial stage, cyclic voltammetry (CV) was carried out on the Zn||V_2O_5 full cell in the blank electrolyte and the electrolyte containing STA, as shown in Fig. 6a and S14.† It can be observed that the reduction peak in the first cycle of the battery has a large shift compared with the reduction peak in the subsequent cycles, which is caused by the formation of the SEI film on the electrode surface during the first discharge. In the subsequent cycles, there was no significant difference between the peak position of the battery after the addition of STA and the battery without the addition of STA, indicating that the introduction of STA had no effect on the redox reaction of the full battery. Fig. 6b and

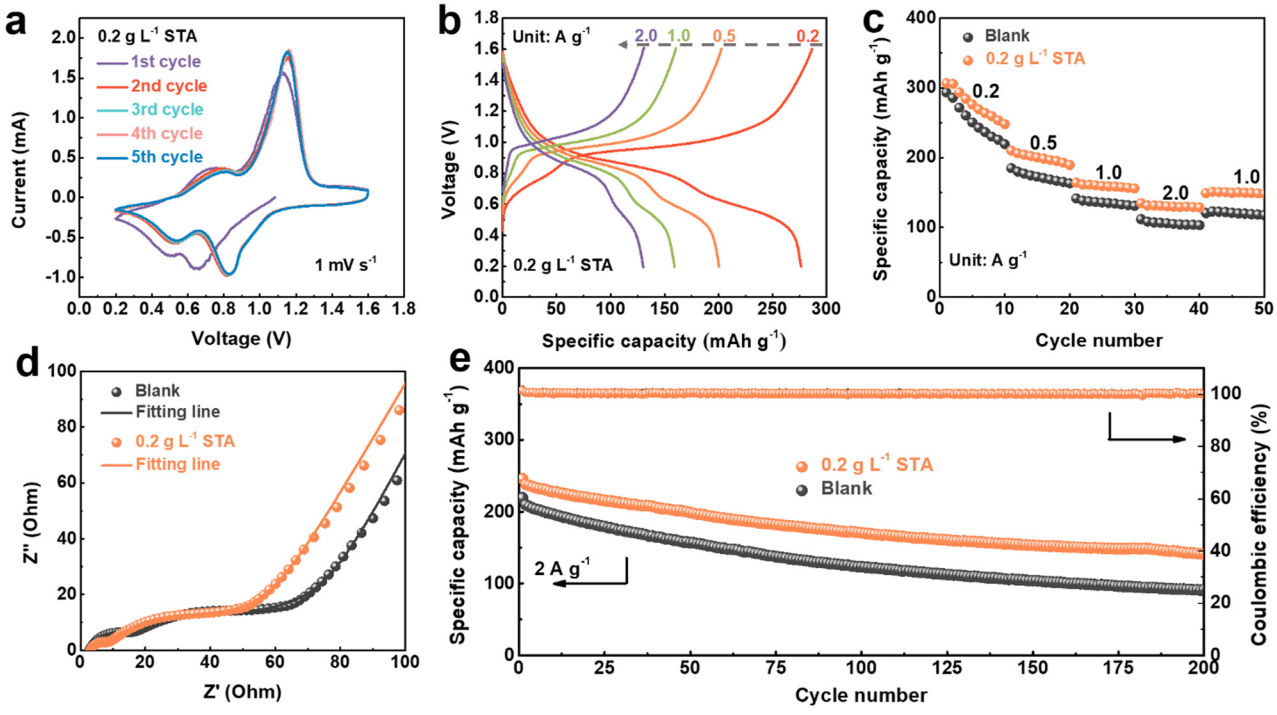

Fig. 6 (a) The CV curves of the Zn||V_2O_5 cells with the STA additive at a scan rate of 1 mV s^{-1}; (b) the discharge/charge curves of the Zn||V_2O_5 cells from 0.2 A g^{-1} to 2 A g^{-1} with the STA additive; (c) rate performance of the Zn||V_2O_5 cells in the electrolyte with/without the STA additive. (d) EIS and fitting curves recorded in the two different electrolytes after 10 cycles; (e) long-term cycling performance of the Zn||V_2O_5 cells in the electrolyte with/without the STA additive at 2 A g^{-1}.

S15† show the charge–discharge profiles of the Zn||V_2O_5 full cell in the blank electrolyte and the electrolyte containing STA, which matches well with the CV curves and still has a stable voltage profile at a current density of 2 A g^{-1}, indicating that the Zn anode has good stability. The rate performance of the Zn||V_2O_5 full cell in both electrolytes is displayed in Fig. 6c. The average specific capacity of the Zn||V_2O_5 full cell containing STA is 280, 200, 150, and 120 mA h g^{-1} at the current density of 0.2, 0.5, 1.0 and 2.0 A g^{-1}, respectively. When the current density returns to 1.0 A g^{-1}, the capacity of 150 mA h g^{-1} can still be maintained, which is superior to the blank electrolyte, demonstrating that the rate performance of the full cell has been improved. This might be a result of the fact that the adsorption layer formed by Zn^{2+} and STA decreases the charge transfer resistance after the introduction of STA, which can also be confirmed by the electrochemical impedance spectroscopy (EIS) measurement of the Zn||V_2O_5 full cell. The equivalent circuit fitting Nyquist curve and the fitting results can be acquired in Fig. S16 and Table S1.† As shown in Fig. 6d, after 10 cycles in the two electrolytes, the interfacial resistance (R_f) and charge-transfer resistance (R_{ct}) of the electrolyte containing STA were both lower than those of the blank electrolyte, suggesting that a stable and uniform electrode–electrolyte interfacial layer was formed after the addition of STA, which promoted charge migration.

The benefits of STA can be further reflected in the long-term cycling stability of the Zn||V_2O_5 full cell (Fig. 6e). The high CE values of both electrolytes at a current density of 2 A g^{-1} are close to 100%. Furthermore, the full cell containing STA maintains a discharge capacity of 142.5 mA h g^{-1} after 200 cycles with a retention rate of 58.0% at 2 A g^{-1}, while the full cell using the blank electrolyte shows dramatic capacity fading with only 40.0% capacity retention, which may be caused by severe dendrite growth and formation of by-products. In addition, the cycle performance of the full battery at 10 °C and 40 °C was also tested, and the battery containing 0.2 g L^{-1} STA performed better than the blank electrolyte (Fig. S17 and S18†).

3 Conclusion

In this study, STA is added to the electrolyte to protect the Zn anode. STA can prevent dendrite as well as H_2 formation, extending the cycle life and durability of ZIBs. The effect mechanism of STA is that STA interacts with Zn^{2+} in the Zn electrode surface, which forms a stable adsorption layer, promotes uniform deposition of Zn^{2+}, and inhibits the growth of dendrites. Additionally, the stronger interaction between STA and Zn^{2+} makes STA replace the water molecules around Zn^{2+} and enter the solvated shell, reducing the occurrence of side reactions, especially H_2 precipitation. It is important to note that it is relatively new to measure the hydrogen precipitation content of a Zn anode submerged in an electrolyte using gas chromatography, which demonstrates intuitively how well STA inhibits hydrogen development. Therefore, Zn||Zn symmetric cells with the STA electrolyte show excellent cycle stability for around 500 h at a current density of 10 mA cm^{-2} and a capacity of 2 mA h cm^{-2}, and Zn||V_2O_5 full cells with the STA electrolyte show long-term cycle stability at a current density of 2 A g^{-1}. To sum up, this work offers a general framework for the future development of high-efficiency and cheap low-cost electrolyte addition.

4 Experimental section

4.1 Materials

Zn foil with a thickness of 0.2 mm (purity of 99.99%) was procured from Suzhou Fosai New Materials Co., Ltd. Zinc sulfate heptahydrate ($ZnSO_4{\cdot}7H_2O$, AR) and vanadium pentoxide (V_2O_5, AR) were purchased from Shanghai Aladdin Bio-Chem Technology Co., Ltd. Sodium tartrate ($C_4H_5O_6Na$) was purchased from Shanghai Macklin Bio-Chem Technology Co., Ltd. A glass fiber separator was supplied by Germany Merck Millipore Co., Ltd.

4.2 Preparation of electrolytes

1 mol L^{-1} $ZnSO_4$ solution as a blank electrolyte was prepared by dissolving zinc sulfate heptahydrate powder in deionized water. Different amounts (1 mg, 2 mg, and 5 mg, respectively) of STA were added to 10 mL of 1 mol L^{-1} $ZnSO_4$ solution to obtain the corresponding concentration of STA followed by 0.1 g L^{-1}, 0.2 g L^{-1}, and 0.5 g L^{-1}. Among them, the optimal concentration of STA was 0.2 g L^{-1}, and its electrolyte was denoted as 1 mol L^{-1} $ZnSO_4$ + 0.2 g L^{-1} STA.

4.3 Material characterization

A scanning electron microscope (SEM, HITACHI SU8010) was used to investigate the surface morphology of the Zn anode. Analysis of element species and content was carried out by energy dispersive spectroscopy (EDS). X-ray photoelectron spectroscopy (XPS) was performed on a Thermo Scientific K-Alpha+ spectrometer (monochromatic Al Kα radiation (1486.6 eV) as an X-ray source) to determine the surface composition of the Zn anode. An FT-IR spectrometer (VERTEX 80v, Bruker) was employed to characterize FT-IR spectra. The ionic conductivity of the electrolyte mentioned above was conducted on a conductivity meter (Shanghai Shiyi Precision Instruments Co., Ltd.). Differential capacitance was tested on an electrochemical comprehensive tester (Solartron 1287) by the electrochemical impedance method (scan rate: 10 mV s^{-1}, potential window: −0.4–0.4 V, frequency: 1000 Hz). The contact angle between the electrolyte and Zn anode was measured using a contact angle meter (JC2000D2A, POWEREACH). The roughness of the surface of the Zn anode after cycling was performed by atomic force microscopy (AFM, Dimension Icon, Bruker). In a mild aqueous electrolyte, hydrogen evolution reactions (HERs) inevitably occur during the battery's resting and charging/discharging process. The decomposition of water molecules in the Zn^{2+} solvated shell can lead to an increase of local OH^-

concentration and the precipitation of hydrogen. The hydrogen evolution device was assembled and the amount of hydrogen precipitation during Zn deposition/stripping was measured using a gas chromatograph (GC9790II). 40 mL of electrolyte was added to a 50 mL test tube, two zinc sheets of the same size welded on a stainless steel column were placed in the electrolyte, and 10 mL of nitrogen gas was passed through. The charging/discharging test was carried out at a certain current density, and the gas in the test tube was extracted at a certain time interval for detection.

4.4 Electrochemical measurements

The electrochemical measurements were conducted by assembling coin-type cells (CR2032), which were composed of a cathode, an anode, the as-prepared electrolyte with/without the STA additive, and a glass fiber separator. Galvanostatic cycling performance tests were carried out in the battery test system (Neware BTS-4000) after 4 hours of rest. The Zn||Zn cells were tested at constant current densities of 2, 5, and 10 mA cm^{-2}, and corresponding area capacities of 4, 2, and 2 mA h cm^{-2}, respectively. The Zn||Cu asymmetric cells were measured to investigate coulombic efficiency (CE). The Zn||V_2O_5 cells were used to test long-term cycling stabilities and life span. For the V_2O_5 synthesis method, it has been reported in previously published literature. V_2O_5 as an active material, Super P as conductive carbon, and PTFE (polytetrafluoroethylene) as a binder were mixed in an ethanol solvent at a mass ratio of 7 : 2 : 1 to obtain a slurry. Then, the slurry was rolled out into slices and tailored into suitable sizes. The active loading masses for the V_2O_5 electrodes were about 2.6 mg cm^{-2}. The Tafel curve which reflects the corrosion behavior of the Zn anode was recorded by scanning in a potential range (±0.3 V) at 1 mV s^{-1} of three-electrode systems. Linear sweep voltammetry (LSV) was performed to figure out the hydrogen evolution reactions (HERs) using Zn||Ti asymmetric cells with a scan rate of 10 mV s^{-1} between −0.3 V and 0 V. The current–time curves reflecting corrosion behavior were collected by the chronoamperometry (CA) method with a voltage of −150 mV over 200 s. Electrochemical impedance spectra (EIS) and cyclic voltammetry (CV) curves were measured using a CHI604E electrochemistry workstation (Shanghai Chen Hua Instrument, Inc.).

4.5 Theoretical calculations

The density functional theory (DFT) calculations were carried out with Gaussian 09. Molecular geometry optimizations and frequency calculations were performed using the B3LYP[63] functional with the D3(BJ) dispersion correction and the def2-SVP[64] basis set for all atoms in the SMD[65] solvation model (H_2O as solvent). The binding energy is defined by the equation as follows: $E_{\text{binding energy}} = E_{\text{complex}} - E_{\text{cation}} - E_{\text{molecular/anion}}$, where E_{complex} is the total energy of the cation–solvent complex, E_{cation} is the total energy of the cation, and $E_{\text{molecular/anion}}$ is the total energy of H_2O or the tartrate ion.

Electronic structure calculations were performed by using the Vienna *ab initio* simulation package (VASP).[66] The generalized gradient approximation (GGA) with the exchange–correlation functional Perdew–Burke–Ernzerhof (PBE) was used. A cutoff energy of 400 eV was employed for the plane-wave basis set, and the projector augmented wave (PAW) method was used to describe core electrons. The convergence criteria for geometry optimization conversion with forces on atoms and energy differences were set to 0.05 eV $Å^{-1}$ and 10^{-4} eV. Under the periodic boundary conditions, the calculations were carried out within a 10.6596 × 10.6596 × 22.4202 $Å^3$ box. For all slabs, a vacuum layer of 15 Å in the Z direction was used to avoid the effect of periodic conditions. The Zn slab (002) used four layers of the 4 × 4 supercell (64 Zn atoms with the bottom two layers fixed) to represent the adsorbed surface. The adsorbed energy of the Zn slab and different species is defined by the equation as follows: $E_{\text{adsorbed energy}} = E_{\text{slab+species}} - E_{\text{slab}} - E_{\text{species}}$, where $E_{\text{slab+species}}$ is the total energy of the optimized adsorbate surface, and E_{slab} and E_{species} are the total energy of the bare surface and adsorbate.

2D models of electrolyte systems were established to simulate the deposition/stripping process of zinc based on COMSOL Multiphysics software. Here the model using the Level Set interface can handle topological changes, thus allowing observation of the entire growth process of electrode boundaries. The complete simulation is characterized as a transient phenomenon where the cathodic boundary continuously shifts, demonstrating the progression of the deposition process. The simulation was executed for a total duration of 700 seconds. The model is 30 μm in length and 65.5 μm in height, with a Zn layer thickness of 5.5 μm at the bottom and an electrolyte thickness of 60 μm. The mesh is chosen to be triangular or tetrahedron-based while using an increasing refinement toward the electrode bands. The cathodic reaction is defined by the Butler–Volmer equation.

Conflicts of interest

There are no conflicts to declare.

Acknowledgements

This work was supported by the National Natural Science Foundation of China (No. 51871113) and the Natural Science Foundation of Jiangsu Province (BK20200047). We thank Tiantian Wu (School of Chemistry, Xi'an Jiaotong University, Xi'an, 710049, China; e-mail: tianwu@xjtu.edu.cn) for his support in theoretical calculations.

References

1 X. Cao, Y. B. Xu, L. F. Zou, J. Bao, Y. X. Chen, B. E. Matthews, J. T. Hu, X. Z. He, M. H. Engelhard, C. J. Niu, B. W. Arey, C. S. Wang, J. Xiao, J. Liu, C. M. Wang, W. Xu

and J. G. Zhang, Stability of solid electrolyte interphases and calendar life of lithium metal batteries, *Energy Environ. Sci.*, 2023, **16**, 1548–1559.

2 M. S. Javed, J. Chen, L. Chen, Y. Xi, C. L. Zhang, B. Y. Wan and C. G. Hu, Flexible full-solid state supercapacitors based on zinc sulfide spheres growing on carbon textile with superior charge storage, *J. Mater. Chem. A*, 2016, **4**, 667–674.

3 P. Z. Mu, C. H. Sun, C. H. Gao, L. Li, H. R. Zhang, J. D. Li, C. C. Li, S. M. Dong and G. L. Cui, Dual network electrode binder toward practical lithium–sulfur battery applications, *ACS Energy Lett.*, 2023, **8**, 3733–3741.

4 C. W. Li, L. Li, B. He, Y. Ling, J. Pu, L. Wei, L. T. Sun, Q. C. Zhang and Y. G. Yao, Roadmap for flexible solid-state aqueous batteries: From materials engineering and architectures design to mechanical characterizations, *Mater. Sci. Eng., R*, 2022, **148**, 100671.

5 J. S. Park, C. H. Jo and S. T. Myung, Comprehensive understanding on lithium argyrodite electrolytes for stable and safe all-solid-state lithium batteries, *Energy Storage Mater.*, 2023, **61**, 102869.

6 H. Pan, Z. B. Cheng, Z. Y. Zhou, S. J. Xie, W. Zhang, N. Han, W. Guo, J. Fransaer, J. S. Luo, A. Cabot and M. Wübbenhorst, Boosting lean electrolyte lithium–sulfur battery performance with transition metals: A comprehensive review, *Nanomicro Lett.*, 2023, **15**, 165.

7 J. Liu, Y. H. Zhang, J. Q. Zhou, Z. K. Wang, P. Zhu, Y. F. Cao, Y. W. Zheng, X. Zhou, C. L. Yan and T. Qian, Advances and prospects in improving the utilization efficiency of lithium for high energy density lithium batteries, *Adv. Funct. Mater.*, 2023, **33**, 2302055.

8 Z. Y. Zhao, F. Q. Chen, J. W. Han, D. B. Kong, S. Y. Pan, J. Y. Xiao, S. C. Wu and Q. H. Yang, Revival of microparticular silicon for superior lithium storage, *Adv. Energy Mater.*, 2023, **13**, 2300367.

9 C. Xing, H. Chen, S. Qian, Z. Wu, A. Nizami, X. Li, S. Zhang and C. Lai, Regulating liquid and solid-state electrolytes for solid-phase conversion in Li-S batteries, *Chem*, 2022, **8**, 1201–1230.

10 S. Nandi, T. K. Goswami and S. K. Das, Al^{3+} ion storage in $LiMnPO_4$ for rechargeable aqueous aluminum-ion battery, *Mater. Lett.*, 2023, **346**, 134513.

11 X. Min, J. Xiao, M. H. Fang, W. Wang, Y. J. Zhao, Y. A. Liu, A. M. Abdelkader, K. Xi, R. V. Kumarb and Z. H. Huang, Potassium-ion batteries: Outlook on present and future technologies, *Energy Environ. Sci.*, 2021, **14**, 2186–2243.

12 C. Vaalma, D. Buchholz, M. Weil and S. Passerini, The demand for lithium-ion batteries (LIBs) has been increasing since their commercialization in 1991 and their widespread use in portable electronics, *Nat. Rev. Mater.*, 2018, **3**, 18013.

13 S. Wang, Q. Wang, W. Zeng, M. Wang, L. M. Ruan and Y. N. Ma, A new free-standing aqueous zinc-ion capacitor based on MnO_2–CNTs cathode and MXene anode, *Nanomicro Lett.*, 2019, **11**, 70.

14 B. Y. Tang, L. T. Shan, S. Q. Liang and J. Zhou, Issues and opportunities facing aqueous zinc-ion batteries, *Energy Environ. Sci.*, 2019, **12**, 3288.

15 J. Yin, H. Yang, Z. Gan, Y. Gao, X. Feng, M. Wang, G. Yang, Y. Cheng and X. Xu, Electron transmission matrix and anion regulation strategy-derived oxygen-deficient δ-MnO_2 for a high-rate and long-life aqueous zinc-ion battery, *Nanoscale*, 2023, **15**, 6353.

16 Z. Q. Wang, M. Zhou, L. P. Qin, M. H. Chen, Z. X. Chen, S. Guo, L. B. Wang, G. Z. Fang and S. Q. Liang, Simultaneous regulation of cations and anions in an electrolyte for high-capacity, high-stability aqueous zinc–vanadium batteries, *eScience*, 2022, **2**, 209–218.

17 J. Cao, D. D. Zhang, X. Y. Zhang, Z. Y. Zeng, J. Q. Qin and Y. H. Huang, Strategies of regulating Zn^{2+} solvation structures for dendrite-free and side reaction-suppressed zinc-ion batteries, *Energy Environ. Sci.*, 2022, **15**, 499–528.

18 R. Guo, X. Liu, F. Xia, Y. Jiang, H. Zhang, M. Huang, C. Niu, J. Wu, Y. Zhao, X. Wang, C. Han and L. Mai, Large-scale integration of a zinc metasilicate interface layer guiding well-regulated Zn deposition, *Adv. Mater.*, 2022, **34**, 2202188.

19 J. Liu, C. Ye, H. Wu, M. Jaroniec and S. Qiao, 2D Mesoporous zincophilic sieve for high-rate sulfur-based aqueous zinc batteries, *J. Am. Chem. Soc.*, 2023, **145**, 5384–5392.

20 J. Cao, D. Zhang, C. Gu, X. Wang, S. Wang, X. Zhang, J. Qin and Z. Wu, Manipulating crystallographic orientation of zinc deposition for dendrite-free zinc ion batteries, *Adv. Energy Mater.*, 2021, **11**, 2101299.

21 S. Zhang, J. Hao, Y. Zhu, H. Li, Z. Lin and S. Qiao, pH-Triggered molecular switch toward texture-regulated Zn anode, *Angew. Chem., Int. Ed.*, 2023, **62**, e202301570.

22 J. Cao, D. Zhang, X. Zhang, Z. Zeng, J. Qin and Y. Huang, Strategies of regulating Zn^{2+} solvation structures for dendrite-free and side reaction-suppressed zinc-ion batteries, *Energy Environ. Sci.*, 2022, **15**, 499–528.

23 D. Feng, Y. Jiao and P. Wu, Proton-reservoir hydrogel electrolyte for long-term cycling Zn/PANI batteries in wide temperature range, *Angew. Chem., Int. Ed.*, 2023, **62**, e202215060.

24 F. Ilyas, J. Chen, Y. Zhang, H. Lu, Y. Huang, H. Ma and J. Wang, Empowering Zn electrode current capability along interfacial stability by optimizing intrinsic safe organic electrolytes, *Angew. Chem., Int. Ed.*, 2023, **62**, e202215110.

25 D. S. Liu, Z. Zhang, Y. Zhang, M. Ye, S. Huang, S. You, Z. Du, J. He, Z. Wen, Y. Tang, X. Liu and C. C. Li, Manipulating OH^--mediated anode-cathode cross-communication toward long-life aqueous zinc-vanadium batteries, *Angew. Chem., Int. Ed.*, 2023, **62**, e202215385.

26 Z. H. Yi, G. Y. Chen, F. Hou, L. Q. Wang and J. Liang, Strategies for the stabilization of Zn metal anodes for Zn-ion batteries, *Adv. Energy Mater.*, 2021, **11**, 2003065.

27 M. Song, H. Tan, D. L. Chao and H. J. Fan, Recent advances in Zn-ion batteries, *Adv. Funct. Mater.*, 2018, **28**, 1802564.

28 T. K. A. Hoang, T. N. L. Doan, K. E. K. Sun and P. Chen, Corrosion chemistry and protection of zinc & zinc alloys by polymer-containing materials for potential use in rechargeable aqueous batteries, *RSC Adv.*, 2015, **5**, 41677–41691.

29 Q. S. Nian, X. R. Zhang, Y. Z. Feng, S. Liu, T. J. Sun, S. B. Zheng, X. D. Ren, Z. L. Tao, D. H. Zhang and J. Chen, Designing electrolyte structure to suppress hydrogen evolution reaction in aqueous batteries, *ACS Energy Lett.*, 2021, **6**, 2174–2180.

30 J. N. Hao, L. B. Yuan, C. Ye, D. L. Chao, K. Davey, Z. P. Guo and S. Z. Qiao, Boosting zinc electrode reversibility in aqueous electrolytes by using low-cost antisolvents, *Angew. Chem., Int. Ed.*, 2021, **60**, 7366–7375.

31 Q. Ma, R. Gao, Y. Liu, H. Dou, Y. Zheng, T. Or, L. Yang, Q. Li, Q. Cu, R. Feng, Z. Zhang, Y. Nie, B. Ren, D. Luo, X. Wang, A. Yu and Z. Chen, Regulation of outer solvation shell toward superior low-temperature aqueous zinc-ion batteries, *Adv. Mater.*, 2022, **34**, e2207344.

32 Z. Hu, F. Zhang, Y. Zhao, H. Wang, Y. Huang, F. Wu, R. Chen and L. Li, A self-regulated electrostatic shielding layer toward dendrite-free Zn batteries, *Adv. Mater.*, 2022, **34**, e2203104.

33 W. Zhang, Y. Dai, R. Chen, Z. Xu, J. Li, W. Zong, H. Li, Z. Li, Z. Zhang, J. Zhu, F. Guo, X. Gao, Z. Du, J. Chen, T. Wang, G. He and I. P. Parkin, Highly reversible zinc metal anode in a dilute aqueous electrolyte enabled by a pH buffer additive, *Angew. Chem., Int. Ed.*, 2023, **62**, e202212695.

34 H. M. Yu, D. P. Chen, Q. Y. Li, C. S. Yan, Z. H. Jiang, L. J. Zhou, W. F. Wei, J. M. Ma, X. B. Ji, Y. J. Chen and L. B. Chen, In situ construction of anode–molecule interface via lone-pair electrons in trace organic molecules additives to achieve stable zinc metal anodes, *Adv. Energy Mater.*, 2023, **13**, 2300550.

35 R. W. Chen, C. Y. Zhang, J. W. Li, Z. J. Du, F. Guo, W. Zhang, Y. H. Dai, W. Zong, X. Gao, J. X. Zhu, Y. Zhao, X. H. Wang and G. J. He, A hydrated deep eutectic electrolyte with finely-tuned solvation chemistry for high-performance zinc-ion batteries, *Energy Environ. Sci.*, 2023, **16**, 2540–2549.

36 L. S. Cao, D. Li, T. Pollard, T. Deng, B. Zhang, C. Y. Yang, L. Chen, J. Vatamanu, E. Y. Hu, M. J. Hourwitz, L. Ma, M. Ding, Q. Li, S. Hou, K. Gaskell, J. T. Fourkas, X. Q. Yang, K. Xu, O. Borodin and C. S. Wang, Fluorinated interphase enables reversible aqueous zinc battery chemistries, *Nat. Nanotechnol.*, 2021, **16**, 902–910.

37 S. Guo, L. P. Qin, T. S. Zhang, M. Zhou, J. Zhou, G. Z. Fang and S. Q. Liang, Fundamentals and perspectives of electrolyte additives for aqueous zinc-ion batteries, *Energy Storage Mater.*, 2021, **34**, 545–562.

38 A. Bayaguud, X. Luo, Y. P. Fu and C. B. Zhu, Cationic surfactant-type electrolyte additive enables three-dimensional dendrite-free zinc anode for stable zinc-ion batteries, *ACS Energy Lett.*, 2020, **5**, 3012–3020.

39 Y. Jin, K. S. Han, Y. Y. Shao, M. L. Sushko, J. Xiao, H. L. Pan and J. Liu, Stabilizing Zinc Anode Reactions by Polyethylene Oxide Polymer in Mild Aqueous Electrolytes, *Adv. Funct. Mater.*, 2020, **30**, 2003932.

40 Z. Hou, H. Tan, Y. Gao, M. H. Li, Z. H. Lu and B. Zhang, Tailoring desolvation kinetics enables stable zinc metal anodes, *J. Mater. Chem. A*, 2020, **8**, 19367–19374.

41 P. He and J. X. Huang, Chemical passivation stabilizes Zn anode, *Adv. Mater.*, 2022, **34**, 2109872.

42 L. T. Kang, M. W. Cui, F. Y. Jiang, Y. F. Gao, H. J. Luo, J. J. Liu, W. Liang and C. Y. Zhi, Nanoporous $CaCO_3$ coatings enabled uniform Zn stripping/plating for long-life zinc rechargeable aqueous batteries, *Adv. Energy Mater.*, 2018, **8**, 1801090.

43 D. Huang, X. L. Zhou, L. M. Liu, H. M. Li, G. Lin, J. Li and Z. H. Wei, Improved electrochemical performance of aqueous zinc-ion batteries with modified glass fiber separator by Ketjen Black, *Colloids Surf., A*, 2023, **663**, 130991.

44 X. X. Liu, W. Wei, Y. F. Yang, Y. J. Li, Y. Li, S. C. Xu, Y. F. Dong and R. H. He, A porous membrane electrolyte enabled by poly(biphenyl piperidinium triphenylmethane) for dendrite-free zinc anode with enhanced cycling life, *Chem. Eng. J.*, 2022, **437**, 135409.

45 A. Mitha, A. Z. Yazdi, M. Ahmed and P. Chen, Surface adsorption of polyethylene glycol to suppress dendrite formation on zinc anodes in rechargeable aqueous batteries, *ChemElectroChem*, 2018, **5**, 2409–2418.

46 Q. Zhang, J. Y. Luan, L. Fu, S. A. Wu, Y. G. Tang, X. B. Ji and H. Y. Wang, The three-dimensional dendrite-free zinc anode on a copper mesh with a zinc-oriented polyacrylamide electrolyte additive, *Angew. Chem., Int. Ed.*, 2019, **58**, 15841–15847.

47 J. Cao, D. D. Zhang, R. Chanajaree, Y. L. Yue, Z. Y. Zeng, X. Y. Zhang and J. Q. Qin, Stabilizing zinc anode via a chelation and desolvation electrolyte additive, *Adv. Powder Mater.*, 2022, **1**, 100007.

48 W. Kao-ian, M. T. Nguyen, T. Yonezawa, R. Pornprasertsuk, J. Qin, S. Siwamogsatham and S. Kheawhom, Highly stable rechargeable zinc-ion battery using dimethyl sulfoxide electrolyte, *Mater. Today Energy*, 2021, **21**, 100738.

49 A. F. Almeida, H. Costa Neto, R. A. C. Santana, J. J. N. Alves, A. R. N. Campos and S. Prasad, Influence of bath composition on the electrodeposition of amorphous Ni-Mo alloys using potassium-sodium tartrate as complexing agent, *Can. J. Chem. Eng.*, 2021, **99**, S284–S294.

50 J. H. Park, S. H. Park, D. Joung and C. Kim, Sustainable biopolymeric hydrogel interphase for dendrite-free aqueous zinc-ion batteries, *Chem. Eng. J.*, 2022, **433**, 133532.

51 X. T. Zhang, J. X. Li, D. Y. Liu, M. K. Liu, T. S. Zhou, K. W. Qi, L. Shi, Y. C. Zhu and Y. T. Qian, Ultra-long-life and highly reversible Zn metal anodes enabled by a desolvation and deanionization interface layer, *Energy Environ. Sci.*, 2021, **14**, 3120–3129.

52 M. Li, K. X. Xie, R. Y. Peng, B. Y. Yuan, Q. H. Wang and C. Wang, Surface protection and interface regulation for Zn anode via 1-hydroxy ethylidene-1, 1-diphosphonic acid electrolyte additive toward high-performance aqueous batteries, *Small*, 2022, **18**, 2107398.

53 H. Bairagi, P. Vashishth, R. Narang, S. K. Shukla and B. Mangla, Experimental and computational studies of a novel metal oxide nanoparticle/conducting polymer

nanocomposite (TiO_2/PVP) as a corrosion inhibitor on low-carbon steel in diprotic acidic medium, *Ind. Eng. Chem. Res.*, 2023, **62**, 10982–11000.

54 J. Y. Qian, H. T. Qin, P. J. Zeng, J. M. Hou, X. S. Mo, G. Shen, H. Zeng, W. T. Zhang, Y. Q. Chen and G. J. Wan, Metal-organic Zn-zoledronic acid and 1-hydroxyethylidene-1,1-diphosphonic acid nanostick-mediated zinc phosphate hybrid coating on biodegradable Zn for osteoporotic fracture healing implants, *Acta Biomater.*, 2023, **166**, 685–704.

55 M. J. D'Ambrose, D. E. Turney, M. N. Nyce, T. N. Lambert, G. G. Yadav and S. Banerjee, Performance advances of industrial-design rechargeable zinc alkaline anodes via low-cost additives, *ACS Appl. Energy Mater.*, 2023, **6**, 6091–6103.

56 M. R. Shaik, S. M. Olidan, J. Kim, K. Y. Cho and S. Yoon, Simultaneous tailoring of hydrogen evolution and dendrite growth via a fertilizer-derived additive for the stabilization of the zinc anode interface, *J. Mater. Chem. A*, 2023, **11**, 6403–6412.

57 C. Huang, X. Zhao, S. Liu, Y. S. Hao, Q. L. Tang, A. P. Hu, Z. X. Liu and X. H. Chen, Stabilizing zinc anodes by regulating the electrical double layer with saccharin anions, *Adv. Mater.*, 2021, **33**, 2100445.

58 P. Sun, L. Ma, W. H. Zhou, M. J. Qiu, Z. L. Wang, D. L. Chao and W. J. Mai, Simultaneous regulation on solvation shell and electrode interface for dendrite-free Zn ion batteries achieved by a low-cost glucose additive, *Angew. Chem., Int. Ed.*, 2021, **60**, 18247–18255.

59 A. Mohammadi, S. Djafer, S. Sayegh, A. J. Naylor, M. Bechelany, R. Younesi, L. Monconduit and L. Stievano, Assessing coulombic efficiency in lithium metal anodes, *Chem. Mater.*, 2023, **35**, 2381–2393.

60 A. K. Patil, U. S. Jagtap and H. R. Talele, Growth and characterization of zinc tartrate crystals in agar-agar gel, *Int. J. Basic Appl. Sci.*, 2022, **11**, 86–90.

61 S. S. Qian, H. Chen, M. T. Zheng, Y. X. Zhu, C. Xing, Y. H. Tian, P. Yang, Z. Z. Wu and S. Q. Zhang, Complementary combination of lithium protection strategies for robust and longevous lithium metal batteries, *Energy Storage Mater.*, 2023, **57**, 229–248.

62 C. F. Liu, Y. Zhang, H. H. Cheng, X. X. Cai, D. Z. Jia and H. Lin, "Dual-engineering" strategy to regulate $NH_4V_4O_{10}$ as cathodes for high-performance aqueous zinc ion batteries, *Small*, 2023, **19**, 2301870.

63 (*a*) A. D. Becke, Density-functional exchange-energy approximation with correct asymptotic behavior, *Phys. Rev. A: At., Mol., Opt. Phys.*, 1988, **38**, 3098; (*b*) C. Lee, W. Yang and R. G. Parr, Development of the Colle-Salvetti Correlation-Energy Formula into a functional of the electron density, *Phys. Rev. B: Condens. Matter Mater. Phys.*, 1988, **37**, 785; (*c*) A. D. Becke, Density-Functional Thermochemistry. III. The role of exact exchange, *J. Chem. Phys.*, 1993, **98**, 5648–5652.

64 F. Weigend and R. Ahlrichs, Balanced basis sets of split valence, triple zeta valence and quadruple zeta valence quality for H to Rn: Design and assessment of accuracy, *Phys. Chem. Chem. Phys.*, 2005, **7**, 3297–3305.

65 A. V. Marenich, C. J. Cramer and D. G. Truhlar, Universal solvation model based on solute electron density and on a continuum model of the solvent defined by the bulk dielectric constant and atomic surface tensions, *J. Phys. Chem. B*, 2009, **113**, 6378–6396.

66 G. Kresse and J. Furthmuller, Efficiency of ab-initio total energy calculations for metals and semiconductors using a plane-wave basis set, *Comput. Mater. Sci.*, 1996, **6**, 15–50.